Smart Structures and Systems, *Vol. 20, No. 3 (2017) 385-396*
DOI: https://doi.org/10.12989/sss.2017.20.3.385

Operation load estimation of chain-like structures using fiber optic strain sensors

Armen Derkevorkian[*1], Francisco Pena[2a], Sami F. Masri[3b] and W. Lance Richards[4c]

[1]*Jet Propulsion Lab., California Inst. of Technology, 4800 Oak Grove Dr., M/S: 157-410, Pasadena, CA 91109, USA*
[2]*NASA Armstrong Flight Research Center, P.O. Box 273, M/S: 48202A, Edwards, CA, 93523, USA*
[3]*Department of Civil Engineering, Viterbi School of Engineering, Univ. of Southern California, 3620 S. Vermont Ave., KAP210, MC: 2531, Los Angeles, CA 90089, USA*
[4]*NASA Langley Research Center, 4876 Lilly Dr., M/S: 2017, Hampton, VA, 23681, USA*

(Received February 17, 2017, Revised June 9, 2017, Accepted June 26, 2017)

Abstract. The recent advancements in sensing technologies allow us to record measurements from target structures at multiple locations and with relatively high spatial resolution. Such measurements can be used to develop data-driven methodologies for condition assessment, control, and health monitoring of target structures. One of the state-of-the-art technologies, Fiber Optic Strain Sensors (FOSS), is developed at NASA Armstrong Flight Research Center, and is based on Fiber Bragg Grating (FBG) sensors. These strain sensors are accurate, lightweight, and can provide almost continuous strain-field measurements along the length of the fiber. The strain measurements can then be used for real-time shape-sensing and operational load-estimation of complex structural systems. While several works have demonstrated the successful implementation of FOSS on large-scale real-life aerospace structures (i.e., airplane wings), there is paucity of studies in the literature that have investigated the potential of extending the application of FOSS into civil structures (e.g., tall buildings, bridges, etc.). This work assesses the feasibility of using FOSS to predict operational loads (e.g., wind loads) on chain-like structures. A thorough investigation is performed using analytical, computational, and experimental models of a 4-story steel building test specimen, developed at the University of Southern California. This study provides guidelines on the implementation of the FOSS technology on building-like structures, addresses the associated technical challenges, and suggests potential modifications to a load-estimation algorithm, to achieve a robust methodology for predicting operational loads using strain-field measurements.

Keywords: fiber optic sensors; strain-field measurements; experimental models; smart buildings; load prediction; condition assessment

1. Introduction

1.1 Background

Real-time operational-load estimation of structural systems is crucial for various monitoring and control applications. The accurate prediction of applied loads can be very important in many types of structures such as offshore platforms, rotating wind turbines, flying un-manned aerial vehicles, as well as conventional civil structures such as multi-span bridges, high-rise buildings, amongst others. Some of the noteworthy works in the area are the following: Chock and Kapania (2003, 2004) proposed a load updating approach for finite element models. Li and Kapania (2004) presented a load updating approach for finite element models using reduced number of unknown load coefficients. Li and Kapania (2007) studied a load updating method for nonlinear finite element models. White *et al.* (2009) investigated potential methodologies to estimate the wind turbine blade operational loading and deflections with inertial measurements. White *et al.* (2010) proposed a model updating method to evaluate the operational monitoring method for wind turbines. Ahmari and Yang (2013) suggested an inverse analysis method for load identification in plates, considering bounded uncertain measurements. Arsenault *et al.* (2013) reported the development of FBG strain sensor system for structural health monitoring in wind turbines. Wang *et al.* (2014) used FBG sensors to monitor the fatigue performance of full-scale partially prestressed concrete beams. Oh *et al.* (2015) proposed a novel method for monitoring and diagnosing blade health for wind turbines. Ciminello *et al.* (2015) investigated the hinge rotation of a morphing rib using FBG sensors. Bao *et al.* (2016) studied distributed strain and crack sensors to monitor concrete pavement.

Some of the recent developments in the fiber optic strain

∗Corresponding author, Ph.D.
E-mail: Armen.Derkevorkian@jpl.nasa.gov
[a]Aerospace Engineer
E-mail: francisco.pena@nasa.gov
[b]Professor
E-mail: masri@usc.edu
[c]Ph.D.
E-mail: lance.richards-1@nasa.gov

http://www.techno-press.com/journals/sss&subpage=7
ISSN: 1738-1584 (Print), 1738-1991 (Online)

sensing (FOSS) technology have been documented in the literature by Lee *et al.* (2002), Stewart *et al.* (2003), Richards (2004), Stewart et al. (2005), Ko et al. (2007), Emmons (2009), Ko and Richards (2009), and Emmons *et al.* (2010). Lizotte and Lokos (2005) proposed a deflection-based aircraft structural load estimation algorithm and experimentally tested it on the active aeroelastic wing F/A-18 aircraft. Richards and Ko (2010) obtained a patent on a process for using surface strain measurements to obtain operational loads for complex structures. Bakalyar and Jutte (2012) experimentally validated the algorithm proposed by Richards and Ko (2010) using various plate elements.

Richards *et al*. (2012) described various applications of the fiber optic instrumentation. Nicolas *et al*. (2013) used the proposed algorithm to estimate out-of-plane loads of a large-scale carbon-composite wing. Derkevorkian *et al.* (2012, 2013) assessed the viability of the algorithm for control and monitoring applications. Strunter *et al*. (2014) investigated the recovery of strain readings from chirping fiber Bragg gratings in composite overwrapped pressure vessels. Pena *et al*. (2014) evaluated the embedded FBGs in composite overwrapped pressure vessels for strain based structural health monitoring.

Estimating the lateral pressure loads (i.e., wind loads) on tall high-rise buildings is important for design, control, and monitoring applications. There is a paucity of methodologies that can accurately predict the lateral pressure loads on building surfaces. Most of such methodologies are not practical to be implemented on full-scale high-rise buildings. Many studies in the literature address the limitations of current techniques that are used to estimate static equivalent wind loads on tall buildings. Zhou *et al.* (1999) examined two code methods for equivalent static wind load estimation and demonstrate that they may lead to some undesirable load effects. Chen and Kareem (2001) addressed the current design practice for wind load estimation on bridges and shows that the estimated load distributions may not be a physically accurate description of the real applied loads. Zhou *et al.* (2002) pointed out the scatter among the wind loads predicted by various international codes and standards. Tamura *et al*. (2008) presents a guide for numerical prediction of wind loads on buildings. Lou *et al.* (2012) shows an experimental and zonal modeling for wind pressures on double-skin facades of a tall building. Magalhaes and Cunha (2016) assessed the viability of data based approaches to identify the modes of a cable-stayed bridge subjected to various wind conditions.

1.2 Motivation

The recent advancements in the sensing technology allow the use of sophisticated, high-resolution, lightweight Fiber Brag Grating (FBG) strain sensors. These sensors are known for their accuracy and their durability in rough environmental conditions. The Fiber-Optic Strain Sensing (FOSS) technology developed at the NASA Armstrong Flight Research Center utilizes FBG strain sensors within long fibers to achieve a robust monitoring system that can be used for various real-time data sensing applications. The availability of the FOSS technology along with the development of the load-estimation algorithms at the Armstrong Center, combined with the need for a robust data-driven methodology to estimate lateral loads on tall buildings, provide a great opportunity to investigate the viability of adopting the approach to monitor lateral loads acting on buildings.

1.3 Scope

Motivated from the preceding, this study assesses the load-estimation algorithms developed at the NASA Armstrong Flight Research Center combined with the state-of-the-art FOSS strain-sensing technology, to explore their viability for lateral operating-load estimation on tall building-like structures. The section on load-estimation algorithm presents the strain sensing approach and the corresponding load-estimation algorithm that consists of two phases; calibration phase and estimation phase. The section on sensitivity analyses presents the analytical investigation of exact and approximate methodologies for moment calculations in typical frames encountered in buildings. Sensitivity analyses are performed to demonstrate the effects of the relative stiffness between the horizontal and the vertical members, as well as the hight-to-width ratio of the frame, on the calculated moments. Furthermore, analyses are performed to show the effects of uncertainty in section properties on the moment calculations.

The section on finite-element analyses shows the finite-element model of a building structure created and analyzed using finite-element software Femap and the Nastran solver. The section on computational results presents the FEA results of the load-estimation algorithm from various loading cases. The section on design of the experimental test-bed structure describes the experimental test-bed, the instrumentation, and the test apparatus. The section on experimental test results presents sample recorded strain measurements and shows the correlation of the experimental tests with the FEA. The discussion section summarizes the observations from the various parts of this research study and provides a guideline on potential future plans to achieve the desired load-estimation framework.

2. Load estimation algorithm

The load-estimation algorithm depends on obtaining strain measurements using Fiber Bragg Gratings (FBGs). The strain information at a specific location can be calculated by measuring the Bragg wavelength λ_B, as shown in Eq. (1)

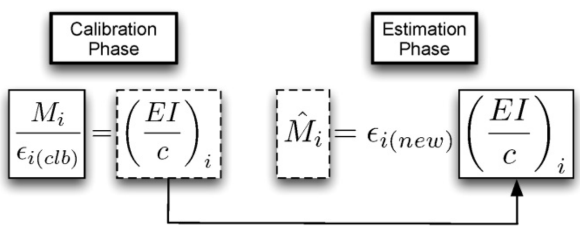

Fig. 1 Flowchart of the load-estimation algorithm for flexure-dominated structure

$$\varepsilon = \frac{1}{(1-p_e)}\left(\frac{\Delta\lambda_B}{\lambda_B}\right) \quad (1)$$

Where ε is the measured strain, p_e is the strain-optic coefficient, λ_B is the Bragg reflected wavelength, and $\Delta\lambda_B$ is the change in the Bragg wavelength. Important works that show the validity of the FBG sensors include Lee *et al*. (2002), Zhou and Sim (2002), Richards (2004), amongst others. As seen in Fig. 1, the load-estimation algorithm developed by Richards and Ko (2010) consists of two phases; calibration phase and estimation phase. During the calibration phase, a known point-load is applied at the tip of the structure and the corresponding strain at each sensor location *i* is measured (i.e., $\varepsilon_{i(clb)}$). For a uniform cantilever beam-like structure, the moment M_i at each location *i* can be computed by multiplying the known point-load at the tip by it's distance from the sensor location *i* (i.e., $M_i = P \times L_i$, where L_i is the distance from the tip of the structure to the location of sensor *i*, and *P* is the point-load applied at the tip (free-end)). The equivalent section property $(EI/c)_i$ at each location *i* can then be estimated by dividing the computed moments M_i by the measured strains $\varepsilon_{i(clb)}$, as shown in Eq. (2)

$$\frac{M_i}{\varepsilon_{i(clb)}} = \left(\frac{EI}{c}\right)_i \quad (2)$$

Where *E* is the Young's modulus, *I* is the moment of inertia, and *c* is the distance from the neutral axis. It should be noted that the algorithm depends on the flexural characteristics of the structure and it assumes the strain is due to bending-only (not shear). It should also be noted that for a more complex structure (i.e., a building consisting of interacting beams and columns with varying stiffness characteristics), the relative stiffness values of the members might be needed to calculate the exact moments needed for the calibration. Further discussion will be provided on this in the upcoming sections.

During the estimation phase, the section properties determined from the calibration phase are used along with the new strain measurements $\varepsilon_{i(new)}$ from new (different) applied loads, to estimate the corresponding moment $\hat{M}_i$, as shown in Eq. (3).

$$\hat{M}_i = \varepsilon_{i(new)} \times \left(\frac{EI}{c}\right)_i \quad (3)$$

If needed, one can then use the moment information to calculate the equivalent distributed load along the fiber line. Estimating the load from the predicted moment is dependent on the characteristics of the applied load (i.e., orientation, type, point load, distributed load, etc.). In their patent, Richards and Ko (2010) demonstrated two loading cases: Point load at the tip of a cantilevered beam, and uniformly distributed load along a cantilevered beam. In most real-life scenarios, it is a daunting task to have this information *a priori*. For example, wind often blows non-uniformly from multiple directions; hence, characterizing the corresponding analytical loading function is a very complex problem. However, having an accurate physics-based moment prediction in it self can be extremely helpful in solving the investigated inverse problem.

The scope of this paper is the investigation of the moment prediction aspect of the methodology, as part of the overall assessment of using FOSS in conjunction with classical mechanics approach. Once the feasibility of the equivalent moment estimation is validated, the authors intend to utilize the algorithm further to estimate the corresponding loads.

3. Sensitivity analyses on analytical moment calculations for calibration phase

As seen in the previous section, an accurate calculation of the moments during the calibration phase is essential for the proposed load-estimation algorithm. In most of the previous studies related to this approach, the testing and the validation was performed on relatively simple structures (i.e., cantilever, uniform and homogeneous beam or plate element). In such structures, the analytical calculation of the moment is relatively simple and can be performed by multiplying the calibration point-load at the free-end of the beam with the distance from the sensor station. No information is needed about the physical characteristics of the beam or the plate (i.e., moment of inertia, stiffness). The objective of this study, as mentioned earlier, is to extend the technique and assess its viability when used with more complex structures, such as buildings with various interacting elements (i.e., beams and columns with varying stiffness characteristics). In the classical theory of structures literature, there are well-established techniques to calculate the moments of statically indeterminate rigid frames. Such techniques include matrix force method, moment distribution method, slope-deflection method, amongst others Hsieh and Mau (2002). In this study the slope-deflection method will be demonstrated symbolically for a one-bay frame. Then, numerical results from the exact solution will be compared to corresponding approximate solutions. The sensitivity of the approximate approach to relative stiffness between horizontal and vertical members, as well as to frame height and width will be analysed.

Let us consider the frame shown in Fig. 2. As seen, the frame consists of one bay. The columns have moment of inertia of I_C and the girder has a moment of inertia of I_G.

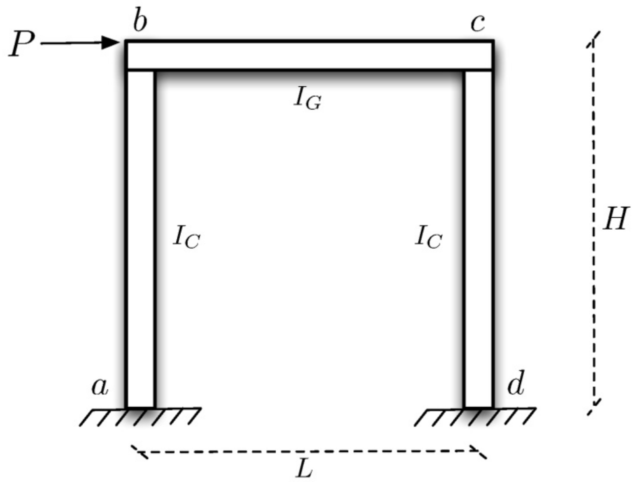

Fig. 2 The sample single-story frame under investigation

The width of the bay is denoted by L, and the height of the frame is denoted by H. A single point-load P is applied at one side of the frame. The frame has four joints denoted by a, b, c, and d. It is assumed that the Young's Modulus of the material for the columns and the girder is E.

Based on the slope-deflection method the moment at each joint (i.e., joint a, M_{ab}) comprises of the moment due to the end rotation θ_a while the other end b is fixed, the moment due to the end rotation θ_b while the other end a is fixed, the moment due to the relative deflection Δ_{ab} between the ends of the member ab, and the moment due to potential loads along the span of the member. In case of the frame shown in Fig. 2, since the bottom supports are fixed, $\theta_a = \theta_d = 0$. Also given the symmetric nature of the frame, $\Delta_{ab} = \Delta_{dc} = \Delta$. Since there are no loads applied on the span of any member, the moment due to loads on span is $M^F = 0$. Therefore the frame-specific moment equations can be written as follows

$$\begin{aligned}
M_{ab} &= \left(\frac{2EI_C}{H}\right)\times\left(\theta_b - \frac{3\Delta}{H}\right)\\
M_{ba} &= \left(\frac{2EI_C}{H}\right)\times\left(2\theta_b - \frac{3\Delta}{H}\right)\\
M_{bc} &= \left(\frac{2EI_G}{L}\right)\times\left(2\theta_b + \theta_c\right)\\
M_{cb} &= \left(\frac{2EI_G}{L}\right)\times\left(2\theta_c + \theta_b\right)\\
M_{cd} &= \left(\frac{2EI_C}{H}\right)\times\left(2\theta_c - \frac{3\Delta}{H}\right)\\
M_{dc} &= \left(\frac{2EI_C}{H}\right)\times\left(\theta_c - \frac{3\Delta}{H}\right)
\end{aligned} \tag{4}$$

The three unknowns (i.e., θ_b, θ_c, and Δ) in the above equations can be solved using the following equations

$$\begin{aligned}
M_{ba} &= M_{bc} = 0\\
M_{cb} &+ M_{cd} = 0\\
P - V_{ab} &- V_{dc} = 0
\end{aligned} \tag{5}$$

where $V_{ab} = (M_{ab} + M_{ba})/H$ and $V_{dc} = (M_{dc} + M_{cd})/H$. The above expressions can be organized in a matrix from as follows

$$K\Theta = F \tag{6}$$

Where

$$K = \begin{bmatrix} 4E\left(\frac{I_C}{H}+\frac{I_G}{L}\right) & 2E\left(\frac{I_G}{L}\right) & -6E\left(\frac{I_C}{H^2}\right)\\ 2E\left(\frac{I_G}{L}\right) & 4E\left(\frac{I_C}{H}+\frac{I_G}{L}\right) & -6E\left(\frac{I_C}{H^2}\right)\\ 6E\left(\frac{I_C}{H^2}\right) & 6E\left(\frac{I_C}{H^2}\right) & -24E\left(\frac{I_C}{H^3}\right) \end{bmatrix} \tag{7}$$

$$\Theta = \begin{bmatrix} \theta_b \\ \theta_c \\ \Delta \end{bmatrix} \tag{8}$$

$$F = \begin{bmatrix} 0 \\ 0 \\ P \end{bmatrix} \tag{9}$$

It is seen that the exact moments of the single-story frame are function of I_C, I_G, H, L, and E.

In some cases, there might be no information available about the physical properties of the frame (such as the moment-of-inertia of the beams and the columns), or performing the exact analytical calculations might take time, especially, for bigger multi-bay multi-story frames with no sophisticated FEA models available. As a result, approximate methods were developed to estimate the moments of the frame. The main assumption with the approximate method is that the inflection point of the member is at the midpoint of the member. Since the inflection point has zero curvature, the bending moment will be zero as well. As a result, one can use statics equations to compute the moments, without incorporating any of the physical characteristics of the member into the equation. For the frame in this example, the approximate moment can be calculated as follows:

$$\hat{M}_a = \hat{M}_b = \frac{P}{2}\times\frac{H}{2} = \frac{P\times H}{4} \tag{10}$$

3.1 Numerical results using exact and approximate methods

In order to better understand the difference between the exact and the approximate solution, and to investigate the sensitivity of the exact approach to the member stiffness and the frame geometry, two numerical examples are presented. In Fig. 3, the sensitivity of the exact solution to the member stiffness is examined. It is seen that as the horizontal member (girder) becomes stiffer, the exact solution approaches the approximate solution. The second subfigure in Fig. 3 shows that if the vertical members are stiffer than the horizontal member, the normalized error between the exact and the approximate solution is about 31% when $I_G = 0.25 \times I_C$. It is also seen that the normalized error decreases to about 4% when $I_G = 5 \times I_C$. This analysis shows that the approximate method can be a viable approach to compute the member moments if the horizontal members are much stiffer than the vertical members (i.e., $I_G \gg I_C$).

Fig. 4 shows the sensitivity of both the exact and the approximate approaches to the frame geometry. This numerical simulation was performed for constant moment-of-inertia values for the horizontal and the vertical members, given by $I_G = 3I_C$. The simulation was performed for various frame heights (with a constant bay width). The first subfigure shows that both the exact and the approximate solutions are relatively similar for M_{ab} and M_{ba}. When looking at the normalized error in the second subfigure, it is seen that as the height-to-width ratio increases, the exact and the approximate solutions converge. Meaning, for tall and slender frames, the approximate solution might provide a good moment estimate (given, the horizontal members are stiffer than the columns).

3.2 Effects of uncertainty on the moment calculations

Let's consider the frame shown in Fig. 5. This is a similar frame to the one analyzed earlier with a slight modification in the section properties. As seen in the figure, the moment-of-inertia for the members ab, bc, and cd are $I_1 \pm \varepsilon_1$, $I_2 \pm \varepsilon_2$, and $I_3 \pm \varepsilon_3$, respectively. The values of I_1, I_2, and I_3 are not necessarily equal. On the other hand, ε_1, ε_2, and ε_3 represent the uncertainty in the moment-of-inertia values. In this case, we assume the width of the bay L and the height of the frame H to be known and deterministic.

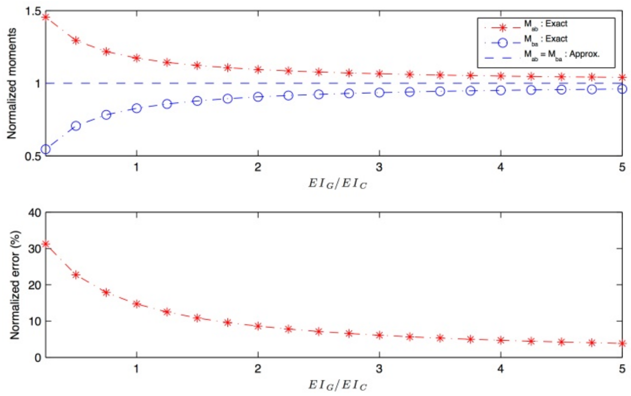

Fig. 3 The first subfigure shows the moments M*ab* and M*ba* for different values of EI_G/EI_C. The exact and the approximate results are superposed. The second subfigure shows the normalized absolute percent error between the exact and the approximate solutions for M*ab*

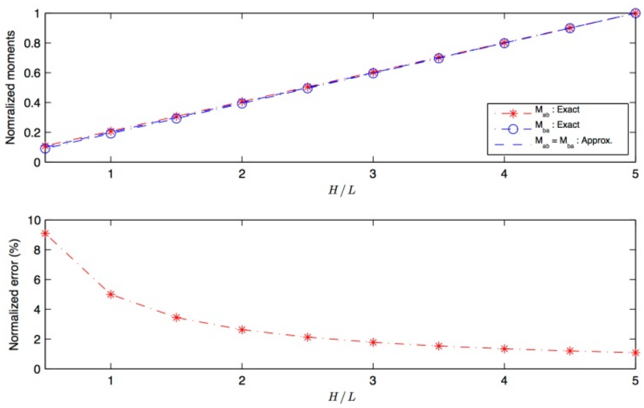

Fig. 4 The first subfigure shows the moments M_{ab} and M_{ba} for different values of H/L when $I_G = 3I_C$. The exact and the approximate results are superposed. The second subfigure shows the normalized absolute percent error between the exact and the approximate solutions for M_{ab}

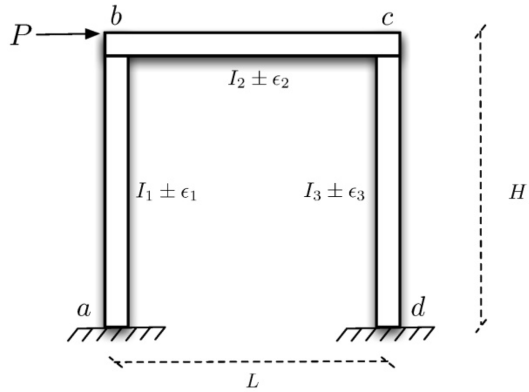

Fig. 5 The sample single-story frame with nondeterministic parameters

Similar to the previous case, a known point-load P is applied on the frame, as shown in Fig. 5.

Taking into account the errors (i.e., uncertainties), the matrix **K** defined earlier, which is used in the moment calculations, is updated as follows

$$K = \begin{bmatrix} 4E\left(\frac{I_1 \pm \varepsilon_1}{H} + \frac{I_2 \pm \varepsilon_2}{L}\right) & 2E\left(\frac{I_2 \pm \varepsilon_2}{L}\right) & -6E\left(\frac{I_1 \pm \varepsilon_1}{H^2}\right) \\ 2E\left(\frac{I_2 \pm \varepsilon_2}{L}\right) & 4E\left(\frac{I_3 \pm \varepsilon_3}{H} + \frac{I_2 \pm \varepsilon_2}{L}\right) & -6E\left(\frac{I_3 \pm \varepsilon_3}{H^2}\right) \\ 6E\left(\frac{I_1 \pm \varepsilon_1}{H^2}\right) & 6E\left(\frac{I_3 \pm \varepsilon_3}{H^2}\right) & -24E\left(\frac{I_1 \pm \varepsilon_1 + I_3 \pm \varepsilon_3}{H^3}\right) \end{bmatrix} \quad (11)$$

In order to assess effects of the uncertain parameters, numerical simulations are performed. The values for ε_1, ε_2, and ε_3 are generated by creating a vector of random numbers that has a zero-mean Gaussian distribution and a standard deviation equal to 10% of the deterministic value of the corresponding moment-of-inertia. Each vector has 2000 samples. For each simulation, all section properties are assumed to be deterministic (i.e., $\varepsilon = 0$) except one moment-of-inertia, which will have normally distributed random values (i.e., $I \pm \varepsilon$). This will show the effects of that uncertain parameter on the accuracy of the calculated moments across the frame. The probability density functions *pdf* of the calculated moments are then estimated using kernel density estimator. Assuming a Gaussian kernel, the bandwidth h of the kernel was chosen to be $h = 1.06\sigma n^{-1/5}$, where σ is the standard deviation of the data and n is the number sample points.

The results from two cases are shown in Figs. 6 and 7. Fig. 6 shows the *pdf*s from the case where $I_1 = I_2 = I_3 = 1$. Each subfigure corresponds to a different moment. In each subfigure, the *pdf*s from three simulations are superposed. Each simulation has a different random variable indicated in the legend. The normalized deterministic exact moment is indicated with a dot on the x-axis. The first subfigure represents the distributions of the moment at point *a* at the bottom of the left column in the frame shown in Fig. 5. As seen, an uncertainty in the section properties of any of the columns, drastically effects the distribution of the calculated moment (i.e., M_{ab}) at that location. On the other hand, the effects of the uncertainty in the girder's properties are not as drastic.

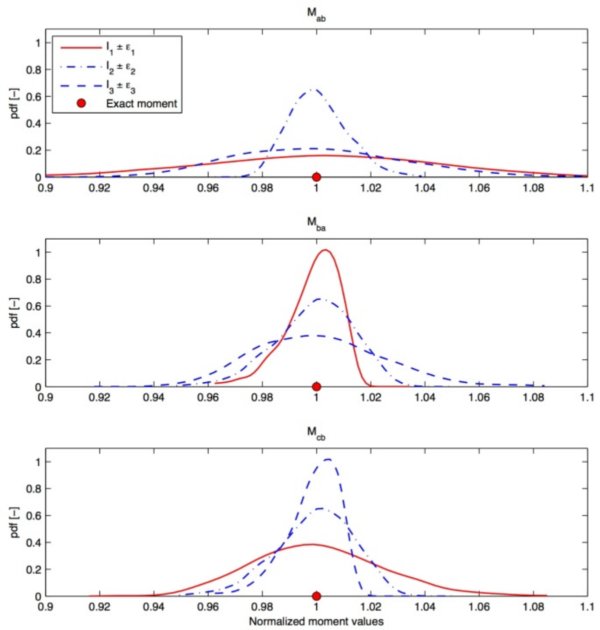

Fig. 6 Normalized probability distribution functions *pdf*s of the calculated moments M_{ab}, M_{ba}, and M_{cb}, where $I_1 = I_2 = I_3 = 1$

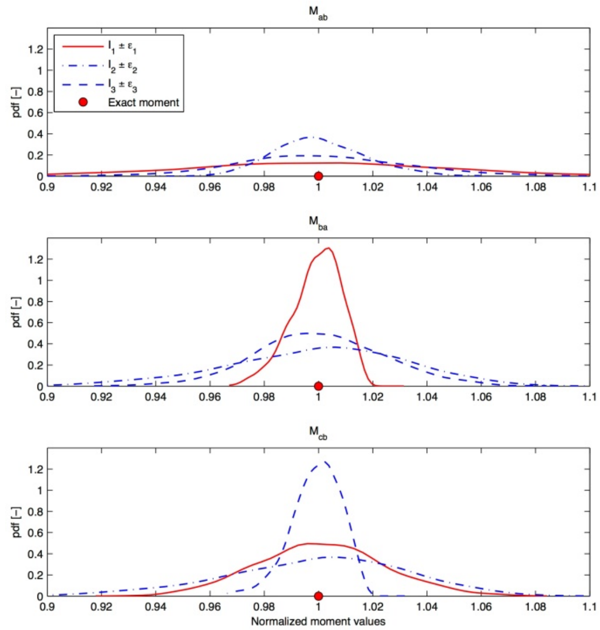

Fig. 7 Normalized probability distribution functions *pdf*s of the calculated moments M_{ab}, M_{ba}, and M_{cb}, where $I_1 = I_3 = 3$ and $I_2 = 1$

Fig. 7 shows simulations from a case where $I_1 = I_3 = 3$ and $I_2 = 1$. This case is similar to strong-column weak-beam condition encountered in most realistic structural frames. Analyzing each of the subfigures can draw similar important information. This analysis shows the importance of taking uncertain parameters into account and their effect on the accuracy of the corresponding moment calculations for the calibration phase in the load-estimation algorithm.

4. Finite Element Analyses (FEA)

4.1 Model description

A finite-element model of a four-story building was created in Femap. The model consists of 2144 combined horizontal and vertical bar elements. The vertical bar elements (columns) are modeled to represent a square tube with dimensions of (2.54 cm ×2.54 cm), a thickness of (0.3175 cm), and a cross-sectional area of (2.83 cm^2). The horizontal bar elements are modeled to have a cross-sectional area of (1.61 cm^2). The material used for the elements is 6061-T651 Aluminum. The width of the frame is (40.64 cm), the height of each floor is (44.45 cm), resulting in a total height of (177.8 cm). Nodal constraints are applied at four nodes at the bottom of the model.

The four nodes are fixed and cannot translate or rotate in any direction (x,y,z).

4.2 Load cases

A total of five load cases are investigated. The load cases under consideration are shown in Fig. 8. The first load case shown in Fig. 8(a) is used for calibration. Two point loads (45.36 kg each) are applied at the tip of the two columns. Both loads are applied in the same negative X-Direction. The purpose of this load case (calibration case) is to obtain the strain measurements and estimate the section properties using the calculated analytical moments. Using the estimated section properties from the calibration load-case, the next four load cases are used for testing.

The second load case (Distributed Point-Loads) is shown in Fig. 8(b). In this case, 8 point loads (45.36 kg each) are applied on two columns (four loads per column).

The loads are all in the same direction. The loads are applied at the intersection of the horizontal members (girders) with the vertical members (columns) at each floor level. The third load case is shown in Fig. 8(c). Point loads are applied at each node on two columns to simulate a pressure load on the two columns. Each point load is 4.53 kg and there are a total of 256 nodes per column. The loads are applied in the same direction.

In order to assess the viability of the algorithm with torsional loads, two load cases were created. The load case named Single-Point-Load (SPL) is shown in Fig. 8(d), where a single point load (45.36 kg) is applied at the tip of one column. The other load case named Moment (TL) is shown in Fig. 8(e), where four moments (1.13 N.m each) are applied (one per floor). The moments are applied to rotate the structure counterclockwise about the Z-Axis. The load cases are summarized in Table 1.

5. Computational results

5.1 Calibration phase

The results from the calibration phase are shown in Fig. 9.

Table 1 The investigated load cases for the four-story building model

Load/Moment Name	Test Code	Number of Loads	Loading Values	Locations
Two Point-Loads (Calibration)	CALIB	2	Two 45.36 kg	Tip (free-end), two columns
Distributed Point-Loads	DL	8	Eight 45.36 kg	Each floor, two columns
Uniform Pressure	PL	n/a	4.53 kg/node	Each node, two columns
Single Point-Load	SPL	1	45.36 kg	Tip (free-end), one column
Moment (Torsion)	TL	4	1.13 N.m	One column, each floor

As mentioned earlier, load case (CALIB) was used on the FEA model to obtain the strain measurements. The presented strain measurements are obtained from the column labeled (1) in Fig. 8(a). The X-Axis in each of the three subfigures of Fig. 9 represents the normalized height of the building starting from zero being the ground (fixed-end) and ending with one being the tip of the building (free-end). The discontinuities seen in the strain and the moment plots are at the location of intersection between the horizontal and the vertical members.

The third subfigure shows the estimated flexural section properties. The column from which the strain data is extracted has uniform section properties along the span; therefore, the estimated *EI/c* values are identical at every sensor station. Of course, this is a highly idealized case (proof of concept) where no uncertainty or modeling errors are involved. More realistic scenarios will be investigated in upcoming studies, taking into account uncertain parameters and modeling errors.

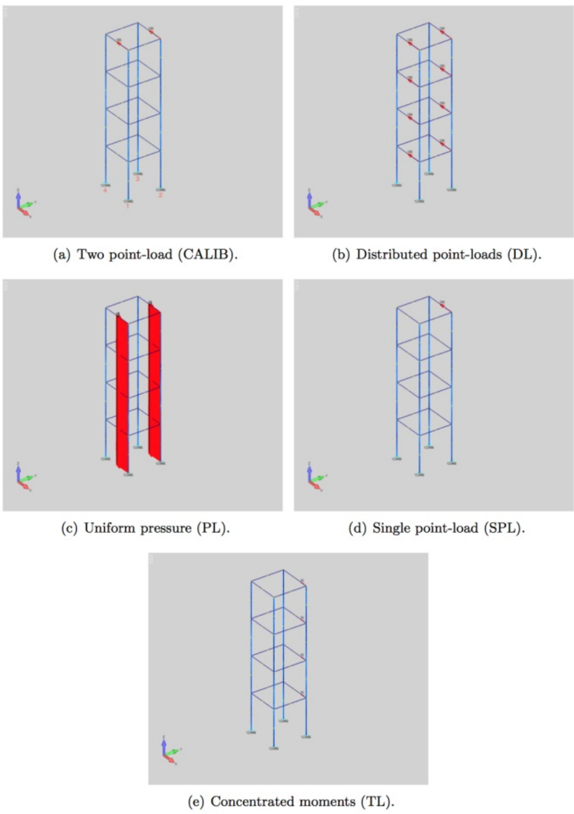

Fig. 8 Description of the five loading cases

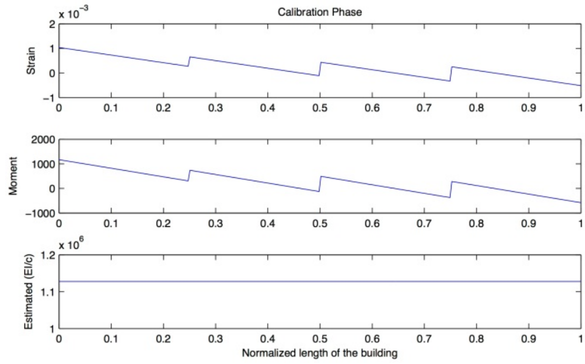

Fig. 9 Strains and moments from the calibration load case, and the estimated section properties

5.2 Estimation phase

Using the section properties estimated in the calibration phase, the remaining four loading cases are tested. The results are shown in Fig. 10. As expected, the estimation is excellent with bending-only loads (i.e., load cases DL and PL), but not as good when twisting effects are introduced (i.e., load cases SPL and TL). As mentioned earlier, this is due to the fact that the algorithm takes into account strain from bending-only loads. It is seen that as the torsional characteristics of the load increase, the estimation quality decreases (Figs. 10(c) and 10(d)).

6. Design of the experimental test-bed structure

6.1 Description of the experimental test-bed

A relatively large-scale experimental building structure was designed and fabricated at the USC Machine Shop. The photo of the building is shown in Fig. 11(a). The total height of the structure is 182.88 cm and the height of each floor is 44.45 cm. As seen in Fig. 11(a), the building has four floors. All components of the structure is made of aluminum. The columns are made of aluminum tubes. The cross-sectional dimensions of the columns are (2.54 cm × 2.54 cm), with a thickness of 0.476 cm. The plates are also 0.476 cm thick and are made of aluminum. The plates are square-shaped with a dimension of (43.18 cm × 43.18 cm).

The plates are connected to the columns via angle-brackets. Each angle-bracket is connected to the column with two No. 10 bolts arranged diagonally along one face of the angle. The angle's other face is connected to the plate with two No. 10 bolts. No. 10 bolts are also used to connect angle-stiffeners to the plates. These stiffeners are designed to be portable so they can easily be added or removed, when needed. Enlarged photos of both the angle-brackets and the stiffeners are shown in Figs. 12(a) and 12(b). The structure is designed such that it can be connected to a heavy base fixture via four large angle-brackets connected to each column at the bottom of the structure. The large brackets are connected to the columns using M8 bolts. On the other hand, the large brackets will be connected to the base-fixture using 1.27 cm diameter bolts.

6.2 Description of the computational model

In order to augment the experimental studies, a finite-element model of the test-bed structure is created using Femap and is shown in Fig. 11(b). The model consists of 45424 elements and 46346 nodes. The element type used to model most of the horizontal and vertical members are 4-noded quad-shape plate elements. The connecting bolts were modeled using 2-noded line-shape bar elements. The geometry and the material properties were designed to match the physical test-bed structure described earlier. Modal analysis was performed and the corresponding classical and torsional mode shapes are plotted in Figs. 13 and 14. The fundamental natural frequency of the modeled structure is 6.76 Hz. The first torsional frequency is 15.90 Hz. The FOSS system is currently capable of sampling at a rate of up to 50 Hz. The test-bed structure was deigned to have two bending modes and two torsional modes below 50 Hz.

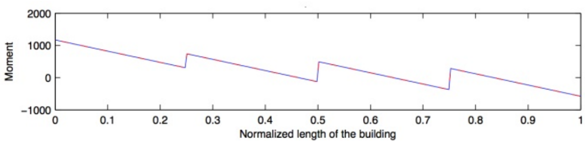

(a) Distributed point-loads (DL).

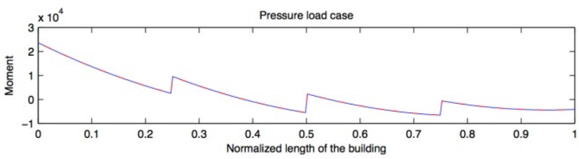

(b) Uniform pressure (PL).

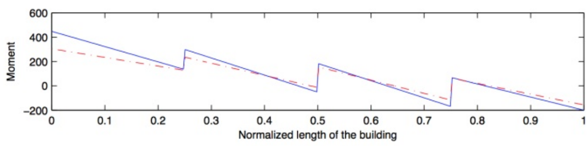

(c) Single point-load (SPL).

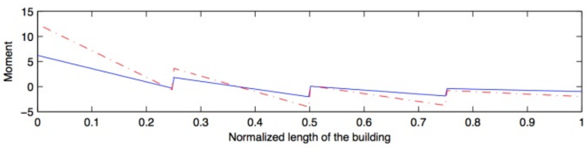

(d) Concentrated moments (TL).

Fig. 10 Estimated moments (dotted line) from various loading cases superposed on the exact analytical moments (solid line) from the FEA

(a) A photo of the four-story experimental test-bed structure.

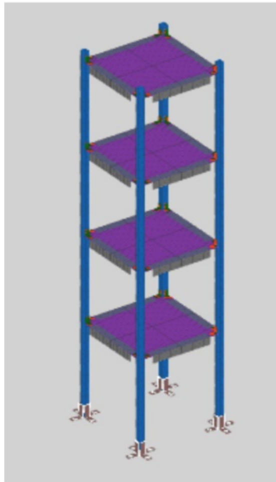

(b) 3D view of the computational model designed in Femap®.

Fig. 11 The experimental and the computational test-bed structure

(a) A sample stiffener attached underneath one of the plates. The angle-brackets used to connect the columns to the plates can be seen on the sides.

(b) Enlarged photo of the bolts and the nuts used to connect the stiffeners to the plates.

Fig. 12 The details of the stiffeners used in the test-bed structure

6.3 Instrumentation and test apparatus

6.3.1 Instrumentation

Installing the fibers on the test-bed is an important part of the experimental test procedure. As shown in Section 5, the load-estimation algorithm currently relies on bending-only (flexural) strains to estimate the corresponding loads. In the same section, it was shown that the estimation quality was not good when dealing with torsional loads. Hence, there is a need to incorporate additional strain information (i.e., shear strain) in the algorithm. In order to capture more complete strain-field information, several fiber configurations were considered. It was seen that the middle of the column-face is the best location for straight fibers to span, because it will capture the most accurate bending-strains. In order to achieve a rosette-effect and capture the shear strain, fibers were also placed at 30-degree angles. Initially, a bending radius of 45 degrees was being considered, but it was found that a 45-degree bending would exceed the allowable bending radius for the fiber.

Accordingly, the fibers are bent at 30-degree angles and there are 8 locations along the span of each column-face where three-component strain information can be measured. Fig. 15(a) shows the fiber locations on the columns. As seen, the fibers will be installed on the outer two faces of each column. As seen in Fig. 15(a) tapes are placed on the columns to depict the geometry of the fibers before installing them. While the fibers are extremely thin, the tapes were designed to provide a 6.35 mm wide pathway to install the fibers. It is worth mentioning that Fiber Bragg Gratings (FBGs) are placed in the fibers at 6.35 mm distance from each other, providing very high spatial-resolution sensors. Photos of the instrumented columns are shown in Fig. 15(b).

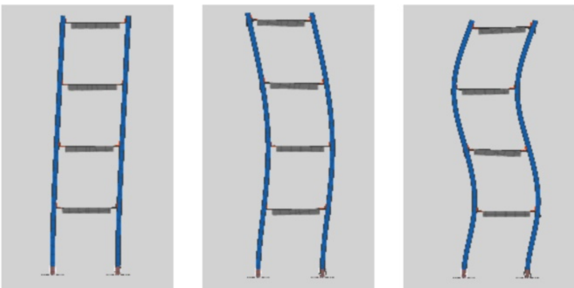

(a) First classical mode shape (6.76 Hz). (b) Second classical mode shape (30.57 Hz). (c) Third classical mode shape (77.18 Hz).

Fig. 13 The classical mode shapes and the corresponding natural frequencies

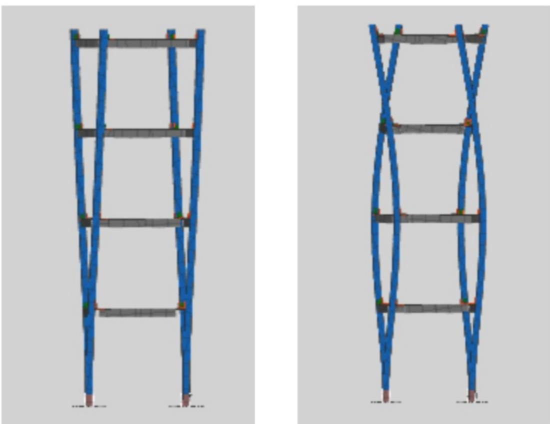

(a) First torsional mode shape (15.90 Hz). (b) Second torsional mode shape (49.33 Hz).

Fig. 14 The torsional mode shapes and the corresponding natural frequencies

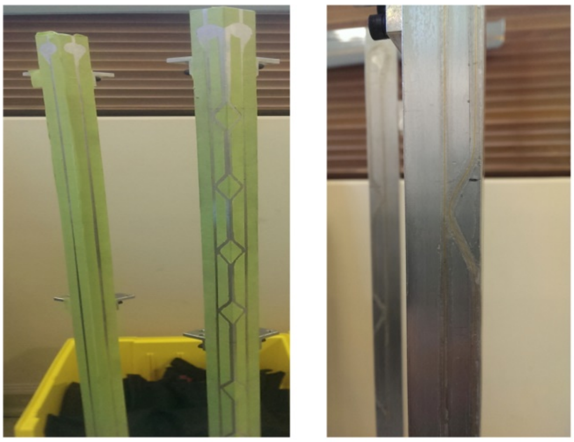

(a) The green tapes used in preparation for fiber-installation. (b) A magnified photo of the installed fibers.

Fig. 15 Location of the fibers installed on the columns of the test-bed structure

6.3.2 Test apparatus

While the ultimate objective of this research is to assess the viability of the approach in predicting random dynamic pressure loads on buildings, the current study concentrates on static loads similar to the ones described in Table 1. In order to apply quasi-static point- loads at various locations on the test-bed structure simultaneously, two pulley-structures were designed and are shown in Fig. 16(a). Furthermore, a base structure was designed to fix the instrumented test-bed structure as well as one of the pulley-structures on it. The dimensions and the spacing of the holes on the base structure were designed to match the angle-brackets at the bottom of the test-bed structure explained earlier. The second pulley-structure was designed to simultaneously apply multi-directional loads on the test- bed and explore the effects of torsional loads. As seen in Fig. 16(a), a 1.83 m tall person is incorporated in the Solidworks model to get a qualitative sense of the overall dimensions of the multiple structures in discussion. The corresponding actual experimental test setup is shown in Fig. 16(b).

7. Experimental test results

Before applying any loads on the test-bed structure, a hammer test was performed to measure the free-vibration response of the structure. The measured strain response was then converted to the frequency-domain using Fast-Fourier-Transform (FFT). Fig. 17 shows the resulting FFT. As seen in the figure, the peak corresponding to the fundamental natural frequency of the structure is at 6.25 Hz. This compares relatively well with the first natural frequency (6.76 Hz) calculated from FEA (shown in Fig. 14(a)).

A sample strain measurement from the distributed load case is shown in Fig. 18. As seen in the figure, the strain discontinuities are clearly depicted in the measurements. The measured strains qualitatively compare well with the FE strains for all load cases. The combination of the observed strain measurements and FFT results indicate that very well correlated computational and experimental models were achieved. An effort is currently underway to use the measured strain datasets from this experiment (both bending strain and shear strain) and to incorporate them into the load-estimation algorithm, to improve its performance when dealing with torsional load cases. The results of the investigation will be reported in upcoming papers.

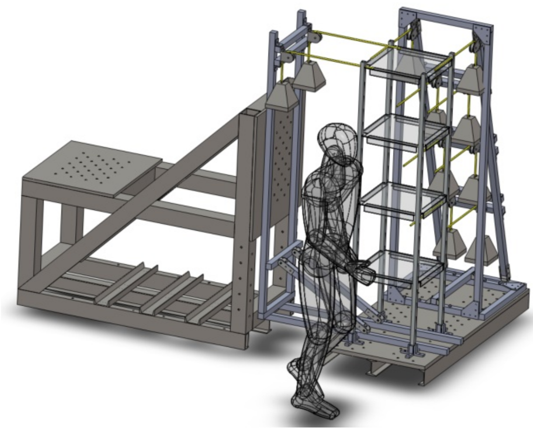

(a) Solidworks model of the test-bed structure

(b) Photo of the actual structure and the pulley system for load application.

Fig. 16 The test-bed structure model and the test apparatus

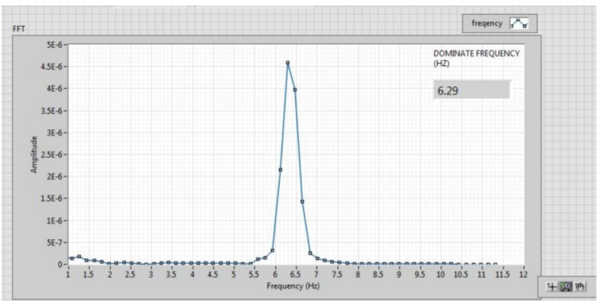

Fig. 17 The calculated FFT using experimental strain measurements form the hammer test

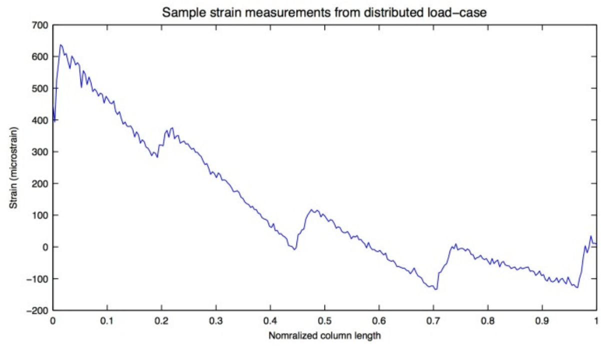

Fig. 18 A sample experimental strain measurement form the distributed load case

8. Conclusions

The load-estimation algorithm under investigation was developed at the NASA Armstrong Flight Research Center providing a robust data-driven model-free approach to estimate operating loads on flexible wing-like aerospace structures. The overall objective of this inaugural effort is to assess the viability of adapting the approach and applying it to chain-like structures, such as tall buildings. The scope of this particular paper is to investigate the moment prediction aspect of the methodology and report on some of the discovered challenges that might arise when using it with building-like structures, such as the effects of strain discontinuities between beams and columns, and sensor topology and bend radius to address torsional loads. Upcoming papers by the authors will focus on resolving the reported challenges in this study and extending the application into predicting operational loads.

With the above summary in mind, the first part of this study concentrated on performing analytical studies of the moment calculations that constitutes a major part of the algorithm. It was shown that the knowledge of the interacting horizontal and vertical members in typical frames, along with their relative section properties, has a big impact on the accuracy of the moment calculations. This is particularly important, since it shows that a priori information is needed for the approach to yield viable estimation results. Approximate moment calculation methods were investigated, where no knowledge is required about the physical characteristics of the frame members; however, it was shown that the results converge to the exact solution only if the horizontal members are much stiffer than the vertical members. In current design practice, most lateral resisting moment frames are geared toward the strong-column weak-beam concept, which further emphasizes that the exact moment calculation methods might be needed for our purposes. Furthermore, a sensitivity analysis was performed on the effects of uncertainty on the moment calculations, and it was shown that an uncertain parameter in a particular frame member might significantly impact the accuracy of the calculated moment in the other frame members.

This paper also pinpoints the discontinuous nature of the strain measurements from building-like structures due to the floor-slabs along their span (or horizontal members such as girders). It was shown that such discontinuities do not affect the accuracy of the load estimation algorithm if the calibration phase is performed properly. However, it is crucial to validate the findings from the computational model by performing experimental analyses.

As mentioned in the previous sections, the load-estimation approach is currently based on bending-only strains for flexural behavior of wing-like structures. A common phenomenon in tall buildings, as well as many other types of structures, is the existence of loads with twisting (torsional) effects. The computational analysis in this study using a finite-element model further emphasizes the importance of having a robust approach that takes into account more complete strain-field information, as opposed to the bending-strains only.

With the above challenges in mind, the final part of this study concentrated on the design of an experimental test-bed structure. Details on the instrumentation, sensor location, sampling frequency, the mode shapes of the test-bed, and the test apparatus for the load application are discussed. The test-bed structure is designed to be used for testing with static loads (as shown in this study), as well as dynamic loads, for future studies. Further experimental testing will shed light on many of the challenges discussed in this study, and will help to develop solutions to overcome them. The load-estimation approach under investigation along with the FOSS sensing technology provide an excellent opportunity to develop a robust framework that can estimate real-time operating loads on variety types of structures, and consequently, have a positive impact on several design, control, and monitoring applications.

Acknowledgments

The assistance of the technicians at the USC Machine Shop and the technical staff at the AERO Institute is highly appreciated. This work was performed and written when the primary author was a research assistant at the University of Southern California. The primary author is currently affiliated with the Jet Propulsion Laboratory, California Institute of Technology.

References

Ahmari, S. and Yang, M. (2013), "Impact location and load identification through inverse analysis with bounded uncertain measurements", *Smart Mater. Struct.*, **22**(8), 085024 (10pp).

Arsenault, T. J., Achuthan, A., Marzocca, P., Grappasonni, C. and Coppotelli, G. (2013), "Development of a FBG based distributed strain sensor system for wind turbine structural health monitoring", *Smart Mater. Struct.*, **22**(7), 075027 (11pp).

Bakalyar, J. and Jutte, C. (2012), "Validation rests of fiber optic strain-based operational shape and load measurements", *Proceedings of the 53rd AIAA/ASME/ASCE/AHS/ASC Structures, Structural Dynamics and Materials Conference*, Honolulu, April.

Bao, Y., Tang, F., Chen, Y., Meng, W., Huang, Y. and Chen, G. (2016), "Concrete pavement monitoring with PPP-BOTDA distributed strain and crack sensors", *Smart Struct. Syst.*, **18**(3), 405-423.

Chen, X. and Kareem, A. (2001), "Equivalent static wind loads for buffeting response of bridges", *J. Struct. Eng. - ASCE*, **127**(12), 1467-1475.

Chock, J.M. and Kapania, R.K. (2003), "Load updating for finite element models", *AIAA J.*, **41**(9), 1667-1673.

Chock, J.M., and Kapania, R.K. (2004), "Finite element load updating for plates", *Proceedings of the 45th AIAA/ASME/AHS/ASCE Structures, Structural Dynamics*, *and Materials Conference*, Palm Springs, CA, April.

Ciminello, M., Ameduri, S., Concilio, A., Flauto, D. and Mennella, F. (2015), "Hinge rotation of a morphing rib using FBG strain sensors", *Smart Struct. Syst.*, **15**(6), 1393-1410.

Derkevorkian, A., Alvarenga, J., Masri, S.F., Ryaciotaki - Boussalis, H. and Richards, W.L. (2012), "Computational studies of a strain-based deformation shape prediction algorithm for control and monitoring applications", *Proceedings of the SPIE Industrial and Commercial Applications of Smart Structures Technologies*, San Diego, March.

Derkevorkian, A., Masri, S.F., Alvarenga, J., Boussalis, H., Bakalyar, J. and Richards, W.L. (2013), "Strain-based deformation shape-estimation algorithm for control and monitoring applications", *AIAA J.*, **51**(9), 2231-2240.

Emmons, M.C., Carman, G.P., Mohanchandra, K.P. and Richards, W.L. (2009), "Characterization and birefringence effect on embedded optical fiber Bragg gratings", *Proceedings of the SPIE Health Monitoring of Structural and Biological Systems*, San Diego, April.

Hsieh, Y. and Mau, S. (1995), Elementary Theory of Structures, (4th Ed.), Prentice-Hall, Upper Saddle River, NJ, USA.

Ko, W. and Richards, W. (2009), "Method for real-time structure shape-sensing", US7520176, United States Patent

Ko, W., Richards, W. and Tran, V. (2007), "Displacement theories for in-flight deformed shape predictions of aerospace structures", NASA/TP-2007-214612, NASA Dryden Flight Research Center, Edwards, CA, United States

Lee, D., Mitrovic, M., Friedman, A., Carman, G. and Richards, L. (2002), "Characterization of fiber optic sensors for structural health monitoring", *J. Compos. Mater.*, **36**(11), 1349-1366.

Li, J. and Kapania, R.K. (2004), "Load updating for finite element models using reduced number of unknown load coefficients", *Proceedings of the 10th AIAA/ISSMO Multidisciplinary Analysis and Optimization Conference*, Albany, NY, September.

Li, J. and Kapania, R.K. (2007), "Load updating for nonlinear finite element models", *AIAA J.*, **45**(7), 1444-1458.

Lizotte, A. and Lokos, W. (2005), "Deflection-based aircraft structural loads estimation with comparison to flight", *Proceedings of the 46th AIAA/ASME/ASCE/AHS/ASC Structures, Structural Dynamics and Materials Conference*, Austin, April.

Lou, W., Huang, M., Zhang, M. and Lin, N. (2012), "Experimental and zonal modeling for wind pressures on double-skin facades of a tall building", *Energ. Buildings.*, **54**, 179-191.

Magalhaes, F. and Cunha, A. (2016), "Automated identification of the modal parameters of a cable- stayed bridge: Influence of the wind conditions", *Smart Struct. Syst.*, **17**(3), 431-444.

Nicolas, M.J., Sullivan, R.W. and Richards, W.L. (2013), "Fiber bragg grating strains to obtain structural response of a carbon composite wing", *Proceedings of the ASME 2013 Conference on Smart Materials, Adaptive Structures, and Intelligent Systems*, Snowbird, September.

Oh, K.Y., Park, J.Y., Lee, J.S., Epureanu, B.I. and Lee, J.K. (2015), "A novel method and its field tests for monitoring and diagnosing blade health for wind turbines", *IEEE T. Instrum. Meas.*, **64**(6), 1726–1733.

Pena, F., Strunter, S., Richards, W., Piazza, A. and Parker, A. (2014), "Evaluation of embedded FBGs in composite overwrapped pressure vessels for strain based structural health monitoring", *Proceedings of the SPIE Smart Structures and Materials, Nondestructive Evaluation, and Health Monitoring*, San Diego, March.

Richards, W. and Ko, W. (2010), “Process for using surface strain measurements to obtain operational loads for complex structures”, US7715994, United States Patent

Richards, W.L. (2004), “Characterization of embedded fiber optic sensors in advanced composite materials for structural health monitoring”, *Proceedings of the SPIE Smart Structures and Integrated Systems*, San Diego, March.

Richards, W., Parker, A., Ko, W.L., Piazza, A. and Chan, P. (2012), “Application of Fiber Optic Instrumentation”, RTO-AG-160-Vol-22, NATO Research and Technology Organization, Systems Concepts and Integration Panel, Paris, France.

Stewart, A., Carman, G. and Richards, L. (2003), “Nondestructive evaluation technique utilizing embedded thermal fiber optic sensors”, *J. Compos. Mater*., **37**(24), 2197-2206.

Stewart, A., Carman, G. and Richards, L. (2005), “Health monitoring technique for composite materials utilizing embedded thermal fiber optic sensors”, *J. Compos. Mater*., **39**(3), 199-213.

Stewart, A., Carman, G. and Richards, L. (2010), “Strain measurement validation of embedded fiber bragg gratings”, *Int. J. Optomechatronics*, **4**(1), 22-33.

Strunter, S., Pena, F., Piazza, A., Parker, A., Richards, W. and Carman, G. (2014), “Recovering strain readings from chirping fiber bragg gratings in composite overwrapped pressure vessels”, *Proceedings of the SPIE Industrial and Commercial Applications of Smart Structures Technologies*, San Diego, March.

Tamura, T., Nozawa, K. and Kondo, K. (2008), “AIJ guide for numerical prediction of wind loads on buildings”, *J. Wind Eng. Ind. Aerod*., **96**(10-11), 1974-1984.

Wang, L., Han, J. and Song, Y. (2014), “Fatigue performance monitoring of full-scale PPC beams by using the FBG sensors”, *Smart Struct. Syst*., **13**(6), 943-957.

White, J., Adams, D. and Rumsey, M. (2010), “Updating of a wind turbine model for the evaluation of methods for operational monitoring using inertial measurements”, *Proceedings of the 48th AIAA Aerospace Sciences Meeting, The New Horizons Forum and Aerospace Exposition*, Orlando, January.

White, J., Adams, D., Rumsey, M. and Paquette, J. (2009), “Estimation of wind turbine blade operational loading and deflection with inertial measurements”, *Proceedings of the 47th AIAA Aerospace Sciences Meeting, The New Horizons Forum and Aerospace Exposition*, Orlando, January.

Zhou, G. and Sim, L. (2002), “Damage detection and assessment in fibre-reinforced composite structures with embedded fibre optic sensors - review”, *Smart Mater. Struct*., **11**, 925-939.

Zhou, Y., Gu, M. and Xiang, H. (1999), “Alongwind static equivalent wind loads and responses of tall buildings. Part I: Unfavorable distributions of static equivalent wind loads”, *J. Wind Eng. Ind. Aerod*., **79**(1-2), 135-150.

Zhou, Y., Kijewski, T. and Kareem, A. (2002), “Along-wind Load effects on tall buildings: Comparative study of major international codes and sandards”, *J. Struct. Eng. - ASCE*, **128**(6), 788-796.

FC